Article:
Connolly, DP and Yu, HS orcid.org/0000-0003-3330-1531 (2021) A shakedown limit calculation method for geogrid reinforced soils under moving loads. Geotextiles and Geomembranes, 49 (3). pp. 688-696. ISSN 0266-1144

https://doi.org/10.1016/j.geotexmem.2020.11.009

A shakedown limit calculation method for geogrid reinforced soils under moving loads

Dr D.P. Connolly

- Corresponding author
- d.connolly@leeds.ac.uk,
- 0113 343 6304
- School of Civil Engineering, University of Leeds, UK, LS2 9JT

Prof. H-S. Yu

- H.Yu@leeds.ac.uk
- School of Civil Engineering, University of Leeds, UK, LS2 9JT

Abstract

A method to calculate the elastic shakedown limit of transportation systems (e.g. pavements and railways) supported by geogrid reinforced soils is presented. For the first time, lower-bound shakedown theory is combined with a strength-based geogrid simulation approach, resulting in a rapid method to quantify the benefit of geogrids on the elastic shakedown limit. It allows decoupling of elastic stress generation and shakedown calculations, meaning it is straightforward to implement, and requires minimal computational effort. Therefore it presents a useful tool to optimise geogrid design for transportation structures such as highway pavements and railways. To show

the capability of the method, shakedown limits are calculated for a variety of geogrid configurations using elastic stresses induced by a moving Hertz load. The effect of geogrid depth, soil cohesion, soil friction angle and loading type (normal versus tangential) are investigated for reinforced and non-reinforced soils. It is found that the optimum depth is sensitive to the soil strength properties. Regarding loading, it is shown that for highly tangential loads, shallower geogrids are effective, while for loads with a minimal tangential component, deeper geogrids are effective.

Keywords: Highway Pavement design; Geogrid Reinforced Soil; Shakedown Limit Theory; Moving cyclic Loading; Railway Track subgrade

1. Background

In the field of transport engineering, highway and railroad structures are subject to dynamic cyclic loading due to traffic ((Kermani *et al.*, 2019), (Connolly and Alves Costa, 2020), (Connolly *et al.*, 2020)). This loading condition is more challenging to design for compared to static loading, because designs must account for the residual stresses that develop over a large number of loading cycles. Also, when considering methods to improve the load bearing performance of a transport structure under cyclic loading, geogrids are a common solution ((Dal *et al.*, 2007), (Marolt Čebašek *et al.*, 2018)). However, the interaction between granular particles and geogrid is highly complex and thus challenging to model. Therefore a method is needed to quickly compute the shakedown limit for cyclic loading in the presence of geogrid reinforced sub-bases.

Currently, when analysing a geogrid reinforced highway pavement or railroad structure, a common method is finite element analysis (Hussein and Meguid, 2016). This often

45 involves representing the grid using either a membrane (Kwon, Tutumluer and
46 Konietzky, 2008), bar elements (Karim *et al.*, 2011), or as a homogenous material with
47 anisotropic strength properties (Yu and Sloan, 1997). The grid-soil interface with FE
48 continuum elements can be either fully bonded or use interface elements that add
49 additional frictional strength. A challenge with these approaches is that they are unable
50 to simulate the stabilisation effect generated due to the interlocking between soil
51 particles and the geogrid. This can cause discrepancies between numerical simulation
52 results and field/laboratory test results. Therefore some researchers, such as (Hatami
53 and Bathurst, 2005) and (Perkins and Edens, 2002), tried artificially increasing the
54 stiffness of the soil and geogrid respectively to increase modelling accuracy.

55 An alternative to finite element modelling, is to use the discrete element method, which
56 has gained increasing attention in recent years ((McDowell *et al.*, 2006), (Ngo, Indraratna
57 and Rujikiatkamjorn, 2016), (Qian *et al.*, 2018)). An advantage of this approach is that
58 individual particles can be simulated. Therefore it overcomes the inability of continuum
59 methods to explicitly model particle-grid interlocking. However, discrete element
60 methods are computationally demanding and require significant calibration. Regardless,
61 (Tutumluer, Huang and Bian, 2012) used the technique to analyse the interlocking
62 behaviour of geogrids with granular materials, while (Tran, Meguid and Chouinard, 2015)
63 showed that geogrid helps stabilise soil. Finally, (Huang *et al.*, 2017) showed that
64 particle rotational resistance has a significant effect on a soil's shear strength.

65 Another approach for geogrid analysis is the use of laboratory testing. For example,
66 (Pasquini *et al.*, 2013) performed shear tests, (Abu-Farsakh and Chen, 2011) performed
67 plate load testing, (Teixeira, Bueon and Zornberg, 2007) performed pull-out tests and (Yu

68 *et al.*, 2019) performed true triaxial testing. In addition, (Liu *et al.*, 2016) used 3D printed
69 replica stone particles with on-board sensors, to analyse the effect of geogrid on rotation
70 during loading, and found that geogrid reinforcement significantly reduced particle
71 rotation. (Lees, 2017) and (Lees and Clausen, 2020) also performed large triaxial
72 compression tests on test samples with and without geogrid reinforcement, with the aim
73 of developing a constitutive model for geogrid reinforced soils. The results were
74 compared against numerical simulations and it was shown that using an apparent
75 cohesion approach was able to more accurately simulate the effect of geogrid compared
76 to the traditional bar elements approach. Therefore, in essence, both the tension
77 membrane and stabilisation effect of the geogrid were both inherently captured within
78 the additional apparent cohesion. This apparent cohesion approach is straightforward
79 to implement within numerical and analytical models.

80 In parallel to developments in geogrid simulation, significant research efforts have also
81 been put into developing shakedown limit approaches for soils ((Werkmeister, Dawson
82 and Wellner, 2004), (Yu and Hossain, 1998)). These are limit analysis approaches,
83 meaning the exact solution is difficult to find, however its 'direct' nature makes it a
84 highly efficient method to approximate the shakedown load limit for an elastic-perfectly
85 plastic soil. In comparison, time marching approaches which account for plastic
86 deformation at each time increment, require significant computational effort.

87 Shakedown analysis is useful for the design of elastic-plastic structures under cyclic
88 loading, considering either static/lower-bound theorem ((Melan, 1938), (Yu, 2006)) or
89 kinematic/upper-bound theorem ((Melan, 1938)). Early approaches were confined to 2D
90 problems, however it was extended to 3D problems more recently (Yu, 2005). It has

gained significant attention in the fields of pavement ((Sharp and Booker, 1984), (Collins, Wang and Saunders, 1993),) and more recently in railroad engineering ((Liu *et al.*, 2018), (Wang *et al.*, 2020), (Connolly *et al.*, 2020) and (Alves Costa, Lopes and Silva Cardoso, 2018)), where it can be used to compute factors of safety and optimise design layer thicknesses.

Considering these parallel advancements in shakedown limit theory and geogrid simulation, this paper combines both to create a method capable of quickly analysing the effect of geogrids on shakedown load limit. Firstly, a shakedown failure criterion based upon Mohr-Coulomb theory is developed. Then a cohesion approach for geogrid modelling is discussed, before combining both to analyse the effect of geogrid depth, soil cohesion and friction angle, and load type on the shakedown limit of geogrid reinforced soil. The method can assist in the design of geogrid reinforced soils for transportation structures (e.g. highway pavements or railroad tracks).

2. Numerical approach

2.1 Lower-bound shakedown theorem

When a highway or railway subgrade is subject to a moving load, it may experience a combination of elastic (recoverable) and plastic (non-recoverable) deformations. Its response to repeated moving loads of constant magnitude can be classified into 4 categories of behaviour, as shown in Figure 1:

1. **Elastic**: The load magnitude is below the material's elastic limit. Material behaviour is fully elastic with no residual strain accumulation, meaning permanent settlement does not occur.

2. **Elastic shakedown**: The load magnitude is at a level that exceeds the material's elastic limit, but is below the elastic shakedown limit. The load therefore causes initial permanent deformation (e.g. minor cracks), however after the build-up of residual stresses, the response returns to elastic again. Further passages do not result in additional permanent settlement.
3. **Cyclic/alternating plasticity**: The load magnitude is greater than the elastic shakedown limit but lower than the plastic shakedown limit. The repeated development of plastic strains often causes failure at a low number of cycles.
4. **Ratcheting:** The load magnitude is greater than the plastic shakedown limit. Plastic strains continue to accumulate with each cycle, resulting in ever-increasing settlement, and the ultimate failure of the structure.

)

The calculation of the elastic shakedown limit is of great interest for structures subject to cyclic loading, and thus the focus of this paper. Using Melan's lower bound shakedown theorem, it is possible to approximate this limit for a 3D structure. Melan's theory states that an elastic-perfectly plastic structure will shakedown (i.e. not fail) under repeated loading, if the yield condition is not validated by any total stress field. This total stress field comprises the self-equilibrated residual stress field, the load induced elastic stress field, and the static stress field. Therefore the goal of shakedown limit analysis is to find the maximum stress field that doesn't violate the yield criterion.

For a linear system, if we apply a unit load, p_0, then using a dimensionless load scaling parameter λ, the shakedown limit load will be equal to, $\lambda p_0 = \lambda$. Melan's shakedown theorem then requires:

$$f\left(\lambda\sigma_{ij}^{e} + \sigma_{ij}^{0} + \sigma_{ij}^{r}\right) \leq 0$$

Where $\lambda\sigma_{ij}^{e}$ is the elastic stress field due to the applied load λp_0. i and j subscripts define the coordinate inside the plane of the half-space under consideration, where i is the vertical direction and j is the direction of load movement. σ_{ij}^{0} is the static stress induced by the structure's self-weight, and σ_{ij}^{r} is the residual stress field. The material yield condition is: $f\left(\sigma_{ij}\right) = 0$. Although the static stress is straightforward to implement (e.g. (Alves Costa, Lopes and Silva Cardoso, 2018)), it typically only has a minor effect on the shakedown limit for highway applications. Therefore the theorem can be simplified:

$$f\left(\lambda\sigma_{ij}^{e} + \sigma_{ij}^{r}\right) \leq 0$$

2.2 Shakedown analysis

Residual stresses are due to plastic deformation, and unlike elastic stresses, do not disappear after a wheel load has passed. The underlying concept behind shakedown analysis is to find a residual stress field that:

1. Allows the structure to resist further yielding compared to the elastic limit
2. Satisfies the equilibrium condition
3. Satisfies the yield condition

Therefore the aim of the lower-bound theorem is to find the maximum possible load scaling parameter that for which a self-equilibrated residual stress field can be found, which also ensures the total stress state lies within the failure criterion.

Consider a moving load with constant speed on the surface of a 3D half-space (Figure 2), where x is the direction of load movement, y is perpendicular to the direction of movement, and z is the vertical direction. Treating tensile stresses as positive, there are 6 possible elastic stress (σ^e) components generated during movement: 3 normal stress directions: σ^e_{xx}, σ^e_{yy}, σ^e_{zz}, and 3 shear stress directions: σ^e_{xy},σ^e_{yz},σ^e_{xz}. Assuming the critical plane is directly below the load, the only shear stress generated in this plane is, σ^e_{xz}, meaning σ^e_{xy}, σ^e_{yz} are zero. Furthermore, because the load is travelling in the x direction, the stresses in the y direction are always intermediate stresses, meaning this is not a critical plane either. Therefore it is possible to consider the total elastic stress field as having just 3 stress components: $\sigma^e_{xx}, \sigma^e_{zz}, \sigma^e_{xz}$.

Using a similar process of deduction for the residual stresses (σ^r), if the load did not induce $\sigma^e_{xy}\ and\ \sigma^e_{yz}$ elastic stresses on the plane, corresponding residual stresses will not remain after passage either. Also, residual stress in the σ^r_{yy} direction will be an intermediate residual stress. To satisfy equilibrium in the vertical direction, residual stresses in the vertical σ^r_{zz} direction cannot occur, while the antisymmetric nature of σ^e_{xz} means that residual stresses cannot be induced. Therefore we can consider the total residual stress field as having just one component: σ^r_{xx}. In terms of total stress, the stress fields are then expressed as:

$$\sigma_{xx} = \lambda\sigma^e_{xx} + \sigma^r_{xx}$$

$$\sigma_{zz} = \lambda\sigma^e_{zz}$$

$$\sigma_{xz} = \lambda \sigma_{xz}^{e}$$

In this work, the Mohr-Coulomb yield condition is used, meaning the total stress state must lie within the Mohr-Coulomb failure surface. In terms of principal stresses, this is:

$$(\sigma_1 - \sigma_3) + (\sigma_1 + \sigma_3)\sin\phi - 2c\cos\phi \leq 0$$

Where ϕ is friction angle and c is cohesion. The principal stresses σ_1 and σ_3 are defined as:

$$\sigma_1 = \frac{\sigma_{xx} + \sigma_{zz}}{2} + \sqrt{\left(\frac{\sigma_{xx} - \sigma_{zz}}{2}\right)^2 + \sigma_{xz}^2}$$

$$\sigma_3 = \frac{\sigma_{xx} + \sigma_{zz}}{2} - \sqrt{\left(\frac{\sigma_{xx} - \sigma_{zz}}{2}\right)^2 + \sigma_{xz}^2}$$

Inserting the total stresses defined above gives the following repeatable expressions:

$$\sigma_1 + \sigma_3 = \sigma_x + \sigma_z$$

$$\sigma_1 - \sigma_3 = 2\sqrt{\left(\frac{\sigma_{xx} - \sigma_{zz}}{2}\right)^2 + \sigma_{xz}^2} = \sqrt{(\sigma_{xx} - \sigma_{zz})^2 + 4\sigma_{xz}^2}$$

Inserting the shakedown limit load and residual stresses into these gives:

$$\sigma_1 + \sigma_3 = \lambda \sigma_{xx}^{e} + \sigma_{xx}^{r} + \lambda \sigma_{zz}^{e}$$

$$\sigma_1 - \sigma_3 = \sqrt{(\lambda \sigma_{xx}^{e} + \sigma_{xx}^{r} - \lambda \sigma_{zz}^{e})^2 + 4(\lambda \sigma_{xz})^2}$$

Then, inserting the new repeatable expressions back into the Mohr-Coulomb failure criterion gives:

$$\sqrt{(\lambda\sigma_{xx}^{e}+\sigma_{xx}^{r}-\lambda\sigma_{zz}^{e})^{2}+4(\lambda\sigma_{xz})^{2}}+(\lambda\sigma_{xx}^{e}+\sigma_{xx}^{r}+\lambda\sigma_{zz}^{e})\sin\phi-2c\cos\phi\leq 0$$

Separating the elastic and residual stress components results in the simplification:

$$f=(\sigma_{xx}^{r}+M)^{2}+N\leq 0$$

Where:

$$M=\lambda\sigma_{xx}^{e}-\lambda\sigma_{zz}^{e}+2\tan\phi(c-\lambda\sigma_{zz}^{e}tan\phi)$$

and

$$N=4(1+\tan^{2}\phi)[(\lambda\sigma_{xz}^{e})^{2}-(c-\lambda\sigma_{zz}^{e}\tan\phi)^{2}]$$

In this expression, the residual stress is unknown, making it difficult to calculate the shakedown load factor λ. However, if $N\leq 0$, it is possible to find one possible shakedown load factor that fulfils the condition:

$$\lambda\leq\frac{c}{|\sigma_{xz}^{e}|+\sigma_{zz}^{e}\tan\phi}$$

To compute this, the maximum value of, $|\sigma_{xz}^{e}|+\sigma_{zz}^{e}\tan\phi$, is calculated for all depths due to the moving load passage. Then the minimum value of λ is the initial estimation of the shakedown limit load.

However, this is only one possible solution, and thus not necessarily equal to the critical shakedown load factor. Therefore a second step is required to check whether it is the critical factor, and if not, use an optimisation procedure to better approximate the most critical shakedown load factor. This involves the following steps:

1. Compute the smaller and larger roots of the residual stress field at all j locations, for a given depth (e.g. $i = 1$). The smaller and larger roots respectively are:

$$\sigma_{xx}^{r} = -M_{ij} - \sqrt{N_{ij}}$$

$$\sigma_{xx}^{r} = -M_{ij} + \sqrt{N_{ij}}$$

2. Compute the maximum smaller critical stress value and the minimum larger critical stress value for the given depth.
3. Use either the maximum smaller critical stress or the minimum larger critical stress to determine proximity to the yield condition
4. If the difference between the solution and the yield condition is lower than the desired threshold (e.g. 0.001), then the shakedown limit for this depth can be considered an acceptable solution
5. If the solution is outside the allowable range, use an optimisation procedure to converge the shakedown limit load to an acceptable value. A bisection method is recommended for this as suggested in (Yu and Wang, 2012).
6. The above procedure is repeated for each depth and the critical shakedown limit is then the minimum value across all depths.

More information on the solution procedure can be found in (Yu and Wang, 2012).

2.3 Geogrid simulation

The approach to simulating geogrid follows that outlined in (Lees, 2017). The geogrid is not explicitly modelled, and instead its effect on soil strength is captured via modification of the cohesion properties in the proximity of the geogrid. This has been

shown to be a reasonable assumption through both laboratory testing and numerical modelling (Lees and Clausen, 2020). The cohesion profile with depth for a particular soil requires laboratory testing to determine the maximum value at the geogrid location, and dissipation with vertical distance from the geogrid. Therefore to deploy the method on a large scale, a database of cohesion profiles would require development.

The general approach and input parameters for this work are derived from large triaxial compression tests on samples with 0.5m diameter and 1m height (Lees, 2017). It was shown that this approach was able to more accurately capture the geogrid behaviour compared to the alternative approach of using bar elements within a finite element formulation. An example of a cohesion profile for a soil with geogrid placed at 0.4m below the ground surface is shown in Figure 3. In the absence of reinforcement, the soil's cohesion is 5kPa, however the geogrid locally increases this to a maximum of 15kPa at 0.4m depth. In the regions directly above and below the geogrid, the cohesion increases or decreases at a rate of 50kPa/m until the cohesion plateaus at the non-reinforced value of 5kPa.

2.4. Methodology

A major advantage of combining shakedown limit theory with the cohesion approach for geogrid modelling is that the calculation of elastic stresses can be decoupled from the calculation of the geogrid shakedown load limit. This means that for a given transport problem, the elastic stresses only need to be computed once, for example using a linear elastic finite element approach. Then the elastic stresses can be used independently to compute shakedown load limits for arbitrary geogrid arrangements.

Considering elastic stress computations typically have computational demands orders of magnitude greater than shakedown limit calculations, the proposed approach makes it very fast to compare geogrid designs and find an optimised solution. In comparison, if a time marching numerical approach with Mohr-Coulomb plasticity and bar/membrane elements for the geogrid is used, then every geogrid design permutation requires a potentially computationally demanding simulation. The practical implementation of the proposed approach is shown in Figure 4 and summarised in 3 steps:

1. Compute elastic stresses ignoring the presence of the geogrid
2. Compute geogrid induced cohesion depth profile
3. Use elastic stresses and geogrid induced cohesion profile to compute the shakedown load limit

3. Numerical simulations

3.1 Elastic stress calculation

To show typical results of the proposed approach and to perform an analysis, example 3D elastic stresses in a solid half-space are calculated analytically, due to a sliding circular Hertz load (Figure 2). Normal and tangential loads are considered according to (Hamilton, 1983). Note however that the shakedown method is equally capable of dealing with more complex stress fields, such as those generated in the presence of subgrade layering. These stresses can be computed using techniques such as the finite element method. However, to show the capability of the method and reduce the number of variables under investigation, a homogenous half-space is considered in this work.

If ν is the Poisson's ratio and a is the radius of the circular Hertz load, the response to a normal load (P), except where, $x = y = z = 0$, is:

$$\sigma_{xx}^{e}(x,y,z) = \frac{3P}{2\pi a^3}\left[(1+\nu)z\varphi + \frac{1}{r^2}\left\{-N(x^2+2\nu y^2) - \frac{Mx^2za}{S} + \frac{y^2-x^2}{r^2}\left[(1-\nu)Nz^2 - \frac{1-2\nu}{3}(NS+2AN+a^3) - \nu Mza\right]\right\}\right]$$

$$\sigma_{zz}^{e}(x,y,z) = \frac{3P}{2\pi a^3}\left[-N + \frac{azM}{S}\right]$$

$$\sigma_{xz}^{e}(x,y,z) = \frac{3P}{2\pi a^3}\left[-z\left(\frac{xN}{S} - \frac{xzH}{G^2+H^2}\right)\right]$$

Where the remaining variables are defined in the appendix. For locations where $x = y = 0$, then, $\sigma_{xz}^{e} = 0$. The σ_{xx}^{e} and σ_{zz}^{e} response to a normal load are:

$$\sigma_{xx}^{e}(0,0,z) = \frac{3P}{2\pi a^3}\left[(1+\nu)\left(z\tan^{-1}\left(\frac{a}{z}\right) - a\right) + \frac{a^3}{2(a^2)}\right]$$

$$\sigma_{zz}^{e}(0,0,z) = \frac{3P}{2\pi a^3}\left[\frac{-a^3}{a^2+z^2}\right]$$

For the case of a tangential load (Q), where $Q = uP$, the response at locations, except, $x = y = 0$, is:

$$\sigma_{xx}^{e}(x,y,z) = \frac{3Q}{2\pi a^3}\left[\frac{axM}{r^4}\left\{\left(\frac{3}{2} - \frac{2x^2}{r^2}\right)(S\nu - 2A\nu + z^2) + \frac{x^2z^2}{S} + \frac{7\nu r^2}{4} - 2\nu x^2 + r^2\right\}\right.$$
$$+ \frac{xzM}{r^4}\left\{\left(\frac{3}{2} - \frac{2x^2}{r^2}\right)\left[-\frac{S}{6}(1-2\nu) - \frac{A}{3}(1-2\nu) - \frac{1}{2}(z^2+3a^2)\right]\right.$$
$$\left.\left.+ \frac{a^2x^2}{S} - \frac{\nu r^2}{4} - \frac{7r^2}{4}\right\} - x\left(\frac{\nu}{4}+1\right)\varphi + \frac{4a^3xz}{3r^4}\left(\frac{3}{2} - \frac{2x^2}{r^2}\right)(1-2\nu)\right]$$

297 $$\sigma_{zz}^{e}(x,y,z) = \frac{3Q}{2\pi a^3}\left[\frac{xzN}{2r^2}\left(1 - \frac{r^2+z^2+a^2}{S}\right)\right]$$

298 $$\sigma_{xz}^{e}(x,y,z) = \frac{3Q}{2\pi a^3}\left[\frac{3z\varphi}{2} + \frac{azM}{r^2}\left\{1 + \frac{x^2}{r^2} - \frac{x^2}{S}\right\}\right.$$

299 $$\left. + \frac{N}{r^2}\left\{-\frac{3}{4}(S+2A) + z^2 - \frac{3}{4}a^2 - \frac{1}{4}r^2 + \frac{z^2}{2}\left(\frac{1}{2} - \frac{2x^2}{r^2}\right)\right\}\right]$$

300 At locations where, $x = y = 0$, then, $\sigma_{zz}^{e} = \sigma_{xz}^{e} = 0$. The σ_{xz}^{e} response to a tangential
301 load is:

302 $$\sigma_{xz}^{e}(0,0,z) = \frac{3Q}{2\pi a^3}\left[-a + \frac{3}{2}z\tan^{-1}\left(\frac{a}{z}\right) - \frac{az^2}{2(a^2+z^2)}\right]$$

303 These stress fields are shown graphically in Figure 5 for the cases of a low tangential
304 load (u=0.1) and a high tangential load (u=0.9). Stresses are normalised with respect
305 to the maximum pressure of the Hertz load: $p_0 = 3P/2\pi a^2$, where a is the radius of
306 the circular loading area. When considering Figure 5(a) it is seen that although the
307 vertical stress is unaffected by the tangential load presence, the horizontal stress and
308 the shear stress are magnified. This is also evident in Figure 5(b) which shows the
309 maximum negative component of each stress (i.e. compressional) at each depth. The
310 effect on vertical stress is small, but noticeable, and the horizontal and shear
311 components are quite different at all depths. As depth increases the stresses start to
312 converge.

313 ## 4. Results and analysis

314 Simulations are computed for the case of a non-reinforced soil, and five cases of
315 reinforced soils, with the geogrid placed at: 0.1, 0.2, 0.3, 0.4, 0.5m. The elastic stresses

316 are computed using the equations above, for 11 values of u, in 0.1 increments ranging
317 from 0-1.

318 ## 4.1 Effect of geogrid depth

319 The effect of geogrid depth is analysed using the soil properties from (Lees, 2017), which
320 is a sandy gravel with a cohesion of 0.1kPa and a friction angle of 45°. The cohesion has
321 a maximum of 15KPa at the depth of the geogrid, and decreases at a rate of 50kPa/m, as
322 shown in Figure 6. This results in a maximum geogrid influence zone spanning 0.298m
323 on both sides of the geogrid location, which is consistent with the findings in (Bussert
324 and Cavanaugh, 2010).
325
326 Figure 7 shows the effect of geogrid depth on shakedown load limit, for a range of
327 normal and tangential load combinations. The shakedown limit is normalised with
328 respect to the load as: $\lambda_{normalised} = \lambda p_0 / c$. However, because the cohesion profile
329 with the geogrid changes with depth, the non-reinforced cohesion value is used for
330 normalisation.

331 For the case of a non-reinforced soil, the shakedown limit decreases with increasing
332 tangential loading. When the loading is purely normal, the shakedown limit factor is
333 25.9, and decreases to 2.2 when the tangential load is equal to the normal load.
334 Similar is true for all of the geogrid cases, which have a reduced shakedown limit for
335 increasing tangential loads. However, the depth of geogrid placement also has a
336 significant impact on the shakedown load limit. When placed at a depth of 0.5m below
337 the half-space surface, it offers zero benefit, resulting in the shakedown limit being
338 equal to the non-reinforced condition. For the 0.4m depth, there is a small benefit

339 when the loading is normal, however offers no benefit when the tangential loading
340 coefficient is ≥0.2. This is partly because when the tangential load is high, the stress
341 field is confined more closely to the half-space surface compared to the solely normal
342 load as shown in the previous elastic stress figures.

343 Comparing the cohesion profiles in Figure 6, part of the reason the deeper grids offer
344 minimal cohesion benefits is because the half-space surface is outside their influencing
345 zone. In comparison, the geogrid depths between 0.1-0.3m yield similar shaped curves,
346 and result in shakedown benefits for all loading combinations. However, the 0.3m depth
347 offers the greatest improvement to shakedown limit, while the 0.1m depth gives a
348 reduced benefit compared to the 0.2m case. This can also be explained by Figure 6
349 which shows that although the 0.1-0.2m geogrid cohesion profiles have higher cohesion
350 values at the soil surface, the total depth range of soil they are able to stabilise is
351 reduced due to the presence of the free surface. Therefore, for this particular soil, it can
352 be concluded that the likely optimum depth for geogrid installation is 0.3m. At this
353 depth, if the loading is purely normal, the geogrid increases the factor of safety by 42%,
354 while if u=1 the factor of safety increases by 500%.

355 ## 4.2 Effect of initial cohesion

356 Figure 8 shows the effect of an initial cohesion of 5kPa on cohesion profiles for the
357 same 5 grid depths. Both the maximum cohesion value at the geogrid location, and
358 tapering gradient are the same as the previous 0.1kPa case. However, in contrast to
359 the 0.1kPa case, the zone of influence of the geogrid is reduced due to a higher initial
360 cohesion than previously. This is reflected in Figure 9 where for all load types and
361 geogrid depths, the benefits due to geogrid are reduced compared to Figure 7. It is

362 seen that for low tangential loads, there is a small benefit when the geogrid is placed
363 in the top 0.3m, with the 0.2m depth offering highest performance. However, as the
364 tangential load increases, the benefits of a geogrid at 0.3m become negligible. When
365 placed at 0.2m, there is a similar level of benefit for all load combinations, however for
366 the 0.1m case, the benefits far exceed the other depths at high tangential loads. This
367 result is quite different from the case of initial cohesion 0.1kPa, where the 0.3m depth
368 shows the highest performance across all load combinations.

369

370 ## 4.3 Effect of friction angle

371 Figure 10 shows the shakedown limits for a soil with c=0.1kPa and friction angles of 10^o
372 and 25^o. Compared with Figure 7 (friction angle 45^o) it is seen that an increased
373 friction angle results in a higher shakedown limit load for all cases, including the non-
374 reinforced condition. The general trend is also similar, however when ϕ is low, the
375 0.4m deep grid shows improved performance for low tangential loads. For example,
376 when $\phi=10^o$, there is noticeable benefit for u≤0.4, but when $\phi=45^o$, the benefit is
377 minimal and only for u≤0.2. For all friction angles, in general, the geogrid offers most
378 performance benefit when placed at 0.3m, however this is particularly pronounced as
379 the tangential load increases. Similar is true when placed at 0.1m depth, where it is
380 seen that there is minimal benefit for low tangential loads but a significant benefit at
381 high tangential loads.

382 ## 4.4 Effect of loading type

383 Figure 7, Figure 9 and Figure 10 show the effects of differing soil and geogrid parameters
384 on shakedown limits, for a variety of loading configurations. The differing properties for

385 each of the simulations give rise to different results, however general trends are visible
386 related to the effect of loading type. It is seen that shallower geogrids (e.g. 0.1m) offer
387 best performance when loading is highly tangential (u=1), and have lower impact when
388 the loading is normal. This is particularly true for the soils with higher cohesion.
389 Conversely, deeper geogrids tend to offer the most benefit when the loading is normal,
390 and when placed at a depth greater than 0.4m, have limited benefit for tangential loads.
391 This is because the tangential related stresses are typically confined towards the
392 uppermost part of the soil stratum.
393

394 ## 5. Discussion

395 The analysis shows that geogrids can positively impact the elastic shakedown limit load
396 of soils supporting transport structures. However, grid performance is dependent
397 upon several variables, including the geogrid depth, soil strength parameters, geogrid
398 stabilisation properties and whether the elastic stresses are induced by normal or
399 tangential loading. If the geogrid is not designed correctly, then it may have limited
400 benefit. In particular, regarding loading, the transportation application is important.
401 For example, highway pavements are subject to higher tangential load compared to
402 railways, meaning that if the friction angle is low, then for rail applications, a shallow
403 geogrid might be preferable. However, for a highway pavement application, if the
404 cohesion is low, then a geogrid placed slightly deeper might be optimum, while if the
405 cohesion is high, then a shallower geogrid may offer better performance. This needs
406 to be also considered in view of the loading environment expected, for example near a
407 highway junction increased tangential forces might be expected due to increased
408 accelerating/decelerating.

Conclusions

This paper presents a method to calculate the elastic shakedown limit of geogrid reinforced soils subject to moving loads. The approach combines lower-bound shakedown theory with a novel geogrid simulation approach, resulting in a rapid and straightforward method to quantify the benefit of geogrids on the elastic shakedown limit. To show an example of the methodology, shakedown limits are calculated for a variety of geogrid configurations using example elastic stresses. The effect of geogrid depth, soil cohesion, soil friction angle and loading type (normal versus tangential) are investigated for reinforced and non-reinforced soils. It is found that:

1. The optimum depth of geogrid placement is sensitive to the soil strength properties. Both the effect of friction angle and cohesion on shakedown limit vary depending upon the ratio between tangential and normal loading. Further, for the properties chosen in this work, changes in cohesion accentuated this dependency.
2. For highly tangential loads, shallower geogrids are effective, while for loads with minimal tangential component, deeper geogrids are effective
3. If the grid is too deep, then it may have limited impact on the shakedown limit, and if too shallow, the benefit may also be compromised. For the cases analysed, the optimum depth for increasing the shakedown limit varied between 0.1-0.3m.

Acknowledgements

The Leverhulme Trust (PLP-2016-270) is thanked for providing the support to undertake this work.

References

Abu-Farsakh, M. Y. and Chen, Q. (2011) 'Evaluation of geogrid base reinforcement in flexible pavement using cyclic plate load testing', *International Journal of Pavement Engineering*, 12(3), pp. 275–288. doi: 10.1080/10298436.2010.549565.

Alves Costa, P., Lopes, P. and Silva Cardoso, A. (2018) 'Soil shakedown analysis of slab railway tracks: Numerical approach and parametric study', *Transportation Geotechnics*. Elsevier, 16(July), pp. 85–96. doi: 10.1016/j.trgeo.2018.07.004.

Bussert, F. and Cavanaugh, J. (2010) 'Recent Research and Future Implications of the Actual Behavior of Geogrids in Reinforced Soil', in *Earth Retention Conference*. Available at: http://www.tjyybjb.ac.cn/CN/article/downloadArticleFile.do?attachType=PDF&id=9987.

Collins, I. F., Wang, A. P. and Saunders, L. R. (1993) 'Shakedown in frictional materials under moving surface loads', *Numerical and Analytical Methods in Geomechanics*, 17(3), pp. 165–174.

Connolly, D. P. *et al.* (2020) 'High speed railway ground dynamics: a multi-model analysis', *International Journal of Rail Transportation*. Taylor & Francis, pp. 1–23. doi: 10.1080/23248378.2020.1712267.

452 Connolly, D. P. and Alves Costa, P. (2020) 'Geodynamics of very high speed transport
453 systems', *Soil Dynamics and Earthquake Engineering*. Elsevier Ltd, 130, p. 105982. doi:
454 10.1016/j.soildyn.2019.105982.

455 Dal, M. *et al.* (2007) 'Closure to " Behavior of a Fiber-Reinforced Bentonite at Large
456 Shear Displacements " by Retaining Wall " by Joseph G . Bentler and', *Journal of*
457 *Geotechnical and Geoenvironmental Engineering*, 1(October), pp. 1–7. doi:
458 10.1061/(ASCE)1090-0241(2007)133.

459 Hamilton, G. M. (1983) 'Explicit equations for the stresses beneath a sliding spherical
460 contact', *Proceedings of the Institution of Mechanical Engineers, Part C: Journal of*
461 *Mechanical Engineering Science*, 197(1), pp. 53–59. doi:
462 10.1243/PIME_PROC_1983_197_076_02.

463 Hatami, K. and Bathurst, R. J. (2005) 'Development and verification of a numerical
464 model for the analysis of geosynthethic-reinforced soil segmental walls under working
465 stress conditions', *Canadian Geotechnical Journal*, 42(4), pp. 1066–1085. doi:
466 10.1139/t05-040.

467 Huang, X. *et al.* (2017) 'Implementation of rotational resistance models: A critical
468 appraisal', *Particuology*. Chinese Society of Particuology, 34, pp. 14–23. doi:
469 10.1016/j.partic.2016.08.007.

470 Hussein, M. G. and Meguid, M. A. (2016) 'A three-dimensional finite element approach
471 for modeling biaxial geogrid with application to geogrid-reinforced soils', *Geotextiles*
472 *and Geomembranes*. Elsevier Ltd, 44(3), pp. 295–307. doi:
473 10.1016/j.geotexmem.2015.12.004.

474 Karim, M. R. *et al.* (2011) 'Predicting the long-term performance of a geogrid-
475 reinforced embankment on soft soil using two-dimensional finite element analysis',
476 *Canadian Geotechnical Journal*, 48(5), pp. 741–753. doi: 10.1139/t10-104.

477 Kermani, B. *et al.* (2019) 'Measuring the migration of subgrade fine particles into
478 subbase using scaled accelerated flexible pavement testing–a laboratory study', *Road*
479 *Materials and Pavement Design*, 20(1), pp. 36–57. doi:
480 10.1080/14680629.2017.1374995.

481 Kwon, J., Tutumluer, E. and Konietzky, H. (2008) 'Aggregate base residual stresses
482 affecting geogrid reinforced flexible pavement response', *International Journal of*
483 *Pavement Engineering*, 9(4), pp. 275–285. doi: 10.1080/10298430701582347.

484 Lees, A. (2017) 'Simulation of geogrid stabilisation by finite element analysis', *ICSMGE*
485 *2017 - 19th International Conference on Soil Mechanics and Geotechnical Engineering*,
486 2017-Septe(2014), pp. 1377–1380.

487 Lees, A. S. and Clausen, J. (2020) 'Strength envelope of granular soil stabilized by multi-
488 axial geogrid in large triaxial tests', *Canadian Geotechnical Journal*, 57(3), pp. 448–452.
489 doi: 10.1139/cgj-2019-0036.

490 Liu, S. *et al.* (2016) 'Effect of geogrid on railroad ballast particle movement',
491 *Transportation Geotechnics*. Elsevier Ltd, 9, pp. 110–122. doi:
492 10.1016/j.trgeo.2016.08.003.

493 Liu, S. *et al.* (2018) 'Shakedown for slab track substructures with stiffness variation',
494 *Geotechnical Research*, 5(1), pp. 31–38. doi: 10.1680/jgere.17.00018.

495 Marolt Čebašek, T. *et al.* (2018) 'Full scale laboratory testing of ballast and concrete

496 slab tracks under phased cyclic loading', *Transportation Geotechnics*, 17(September),
497 pp. 33–40. doi: 10.1016/j.trgeo.2018.08.003.

498 McDowell, G. R. *et al.* (2006) 'Discrete element modelling of geogrid-reinforced
499 aggregates', *Proceedings of the Institution of Civil Engineers Geotechnical Engineering*,
500 56(GE1), pp. 35–48. doi: 10.1680/geot.2006.56.9.651.

501 Melan, E. (1938) 'Der spannungsgudstand eines Henky-Mises schen Kontinuums bei
502 Verlandicher Belastung', *Sitzungberichte der Ak Wissenschaften Wie*, 147, p. 73.

503 Ngo, N. T., Indraratna, B. and Rujikiatkamjorn, C. (2016) 'Modelling geogrid-reinforced
504 railway ballast using the discrete element method', *Transportation Geotechnics*.
505 Elsevier Ltd, 8, pp. 86–102. doi: 10.1016/j.trgeo.2016.04.005.

506 Pasquini, E. *et al.* (2013) 'Laboratory characterisation and field validation of geogrid-
507 reinforced asphalt pavements', *Road Materials and Pavement Design*, 14(1), pp. 17–
508 35. doi: 10.1080/14680629.2012.735797.

509 Perkins, S. W. and Edens, M. Q. (2002) 'Finite Element and Distress Models for
510 Geosynthetic-reinforced Pavements', *International Journal of Pavement Engineering*,
511 3(4), pp. 239–250. doi: 10.1080/1029843021000083504.

512 Qian, Y. *et al.* (2018) 'Triaxial testing and discrete-element modelling of geogrid-
513 stabilised rail ballast', *Proceedings of the Institution of Civil Engineers: Ground*
514 *Improvement*, 171(4), pp. 223–231. doi: 10.1680/jgrim.17.00068.

515 Sharp, R. W. and Booker, J. R. (1984) 'Shakedown of pavements under moving surface
516 loads', *Journal of Transportation Engineering*, 110(1), pp. 1–14. doi:
517 10.1061/(ASCE)0733-947X(1984)110:1(1).

Teixeira, S., Bueon, B. and Zornberg, G. (2007) 'Pullout Resistance of Individual Longitudinal and Transverse Geogrid Ribs', *Journal of Geotechnical and Geoenvironmental Engineering*, 1(October). doi: 10.1061/(ASCE)1090-0241(2007)133.

Tran, V. D. H., Meguid, M. A. and Chouinard, L. E. (2015) 'Three-dimensional analysis of geogrid-reinforced soil using a finite-discrete element framework', *International Journal of Geomechanics*, 15(4), pp. 1–19. doi: 10.1061/(ASCE)GM.1943-5622.0000410.

Tutumluer, E., Huang, H. and Bian, X. (2012) 'Geogrid-aggregate interlock mechanism investigated through aggregate imaging-based discrete element modeling approach', *International Journal of Geomechanics*, 12(4), pp. 391–398. doi: 10.1061/(ASCE)GM.1943-5622.0000113.

Wang, K. *et al.* (2020) 'Shakedown analysis of ballasted track structure using three-dimensional finite element techniques', *Acta Geotechnica*. Springer Berlin Heidelberg, 15(5), pp. 1231–1241. doi: 10.1007/s11440-019-00818-6.

Werkmeister, S., Dawson, A. R. and Wellner, F. (2004) 'Pavement design model for unbound granular materials', *Journal of Transportation Engineering*, 130(5), pp. 665–674. doi: 10.1061/(ASCE)0733-947X(2004)130:5(665).

Yu, H. S. (2005) 'Three-dimensional analytical solutions for shakedown of cohesive-frictional materials under moving surface loads', *Proceedings of the Royal Society A: Mathematical, Physical and Engineering Sciences*, 461(2059), pp. 1951–1964. doi: 10.1098/rspa.2005.1445.

Yu, H. S. (2006) *Plasticity and Geotechnics (Advances in Mechanics and Mathematics)*.

Springer. doi: 10.1007/978-1-4613-0247-6.

Yu, H. S. and Hossain, M. Z. (1998) 'Lower bound shakedown analysis of layered pavements using discontinuous stress fields', *Computer Methods in Applied Mechanics and Engineering*, 167(3–4), pp. 209–222.

Yu, H. S. and Sloan, S. W. (1997) 'Finite element limit analysis of reinforced soils', *Computers and Structures*, 63(3), pp. 567–577. doi: 10.1016/S0045-7949(96)00353-7.

Yu, H. S. and Wang, J. (2012) 'Three-dimensional shakedown solutions for cohesive-frictional materials under moving surface loads', *International Journal of Solids and Structures*. Elsevier Ltd, 49(26), pp. 3797–3807. doi: 10.1016/j.ijsolstr.2012.08.011.

Yu, Z. *et al.* (2019) 'True triaxial testing of geogrid for high speed railways', *Transportation Geotechnics*, 20(March). doi: 10.1016/j.trgeo.2019.100247.

Appendix

The repeatable expressions for the elastic stress calculation are:

$A = r^2 + z^2 - a^2$,

$S = (A^2 + 4a^2z^2)$,

$r^2 = x^2 + y^2$,

$M = \sqrt{\frac{S+A}{2}}$,

560 $N = \sqrt{\frac{S-A}{2}}$,

561 $\varphi = \tan^{-1}\left(\frac{a}{M}\right)$,

562 $G = M^2 - N^2 + zM - aN$,

563 $H = 2MN + aM + zN$

564

565

566 Figures

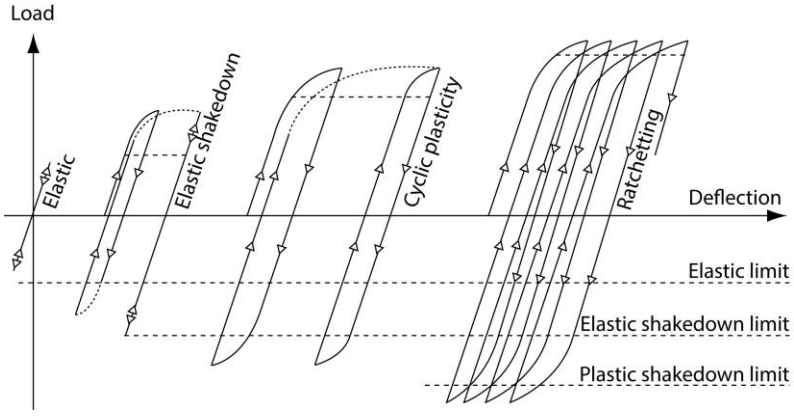

567

568 Figure 1. Elastic-perfectly plastic behaviour during cyclic loading (modified from (Tran,

569 Meguid and Chouinard, 2015)

570

571

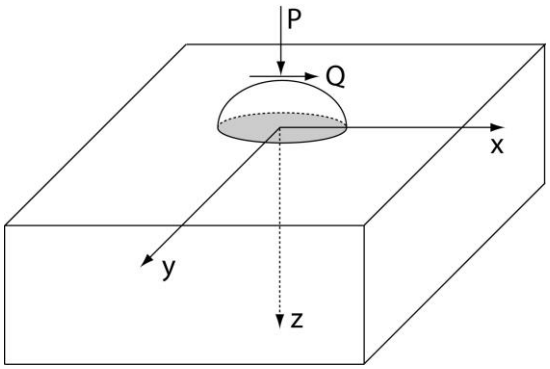

572 *Figure 2. Half-space traversed by a 3D moving Hertz load*

573

574

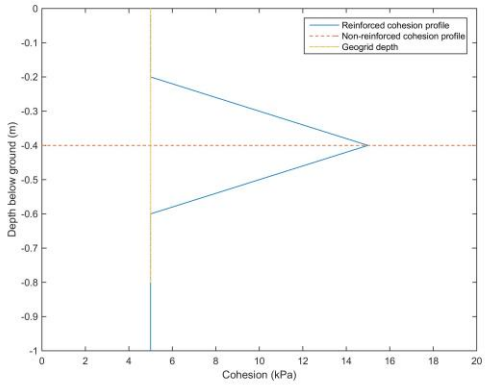

575

576 *Figure 3. Example cohesion profile for a geogrid reinforced soil*

577

578

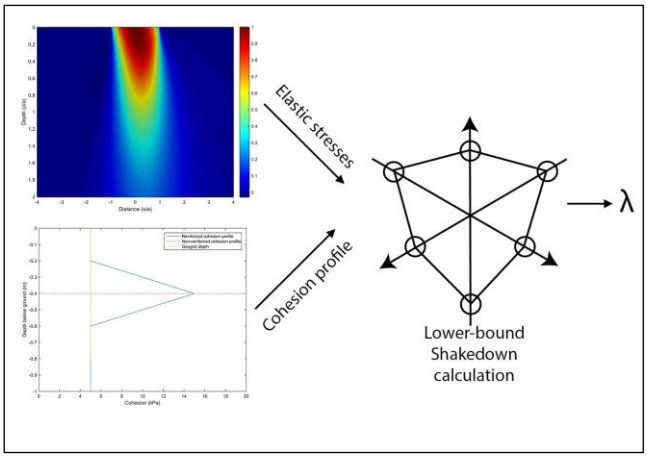

579

580 *Figure 4. Geogrid shakedown calculation process*

581

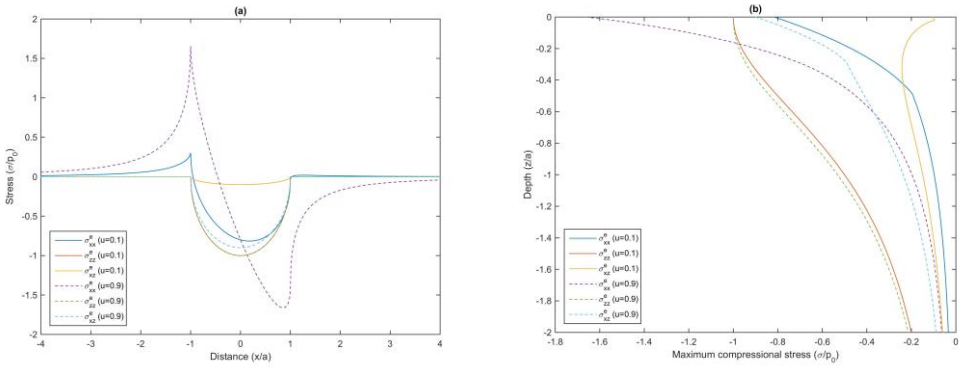

582

583 *Figure 5. Stress plots, (a) Stress contours at half-space surface, (b) Maximum stress with depth*

584

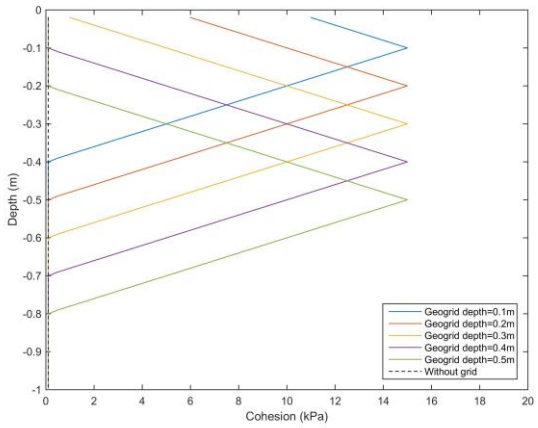

585

586 *Figure 6. Reinforced and non-reinforced cohesion profiles for varying geogrid depths (c=0.1kPa)*

587

588

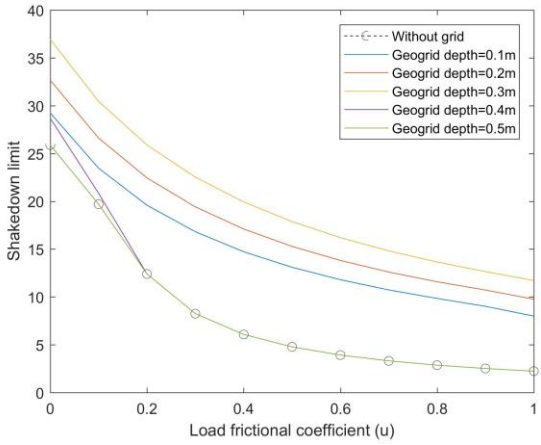

589

590 *Figure 7. Shakedown limits for a sandy gravel (c=0.1kPa, ϕ= 45^o)*

591

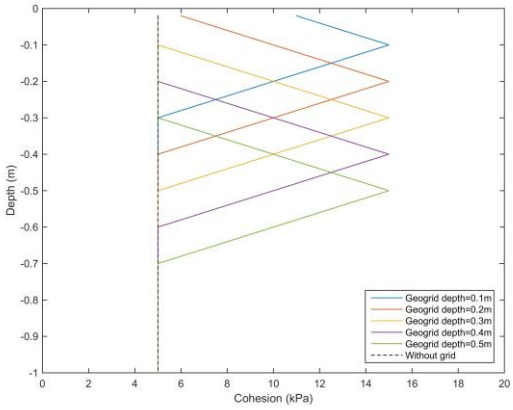

592

593 *Figure 8. Reinforced and non-reinforced cohesion profiles for varying geogrid depths (c=5kPa)*

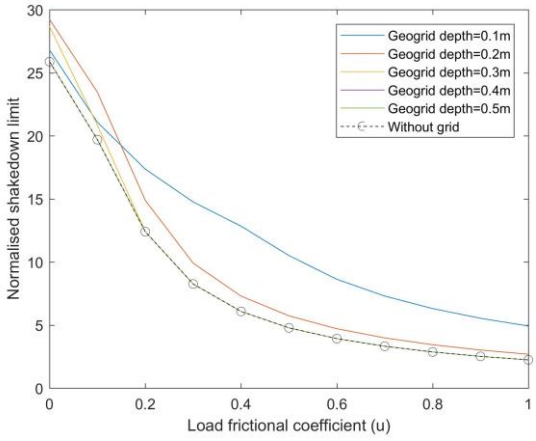

594

595 *Figure 9. Shakedown limits (c=5kPa, ϕ= 45°)*

596

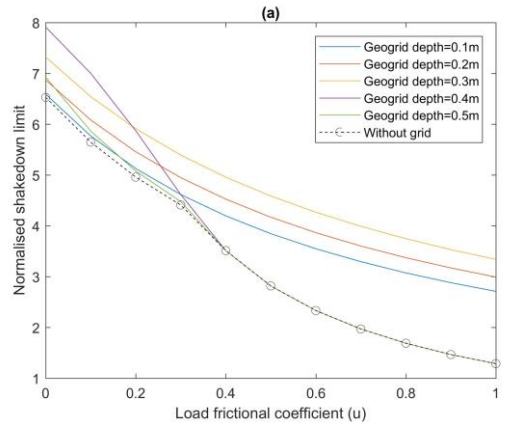

597

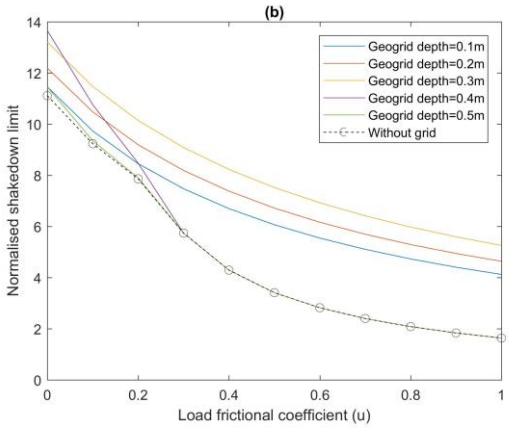

598

599 *Figure 10. Shakedown limits for a soil with c=0.1kPa, (a) friction angle 10^o, (b) friction angle 25^o*

600